Applied Catalysis B: Environmental 332 (2023) 122741

Contents lists available at ScienceDirect

Applied Catalysis B: Environmental

journal homepage: www.elsevier.com/locate/apcatb

Poly(dibenzothiophene-S,S-dioxide)-Fe_2O_3 heterojunction for photocatalytic hydrogen production coupled with selective oxidation of benzyl alcohol

Jun Wu [a], Ye Wang [b,c], Song Zhang [b,c,**], Yuxiang Liu [a], Feng Wang [a,*]

[a] School of Chemical Engineering and Pharmacy, Wuhan Institute of Technology, Wuhan 430205, China
[b] State Key Laboratory of Magnetic Resonance and Atomic and Molecular Physics, Innovation Academy for Precision Measurement Science and Technology, Chinese Academy of Sciences, Wuhan 430071, China
[c] University of Chinese Academy of Sciences, Beijing 100049, China

ARTICLE INFO

Keywords:
Photocatalytic conversion
Z-scheme heterostructures
Selective oxidation
Benzyl alcohol

ABSTRACT

Photocatalytic conversion of benzyl alcohol (BA) into value-added fine chemicals and hydrogen (H_2) in water medium provides a novel strategy for green synthesis. The construction of Z-scheme heterostructures not only realize enhanced charge-separation efficiency, but also remain strong drive force for photocatalytic reaction, which exhibit great potentials toward simultaneously generating benzaldehyde (BAD) and H_2. Herein, we report a noble-metal-free Z-scheme photocatalytic system consisting poly(dibenzothiophene-S,S-dioxide) (PSO) and α-Fe_2O_3 for selective oxidation of BA with synchronous H_2 production. Such nanocomposites can effectively transfer and reduce the recombination of photoexcited charge carriers, therefore maintaining the oxidizability of holes of α-Fe_2O_3 and the reducibility of electrons of PSO. As expected, PSO-Fe_2O_3 with a mass of ~5 mg under optimal composition ratio exhibited an impressive photocatalytic activity with BAD and H_2 yields up to 23.1 and 29.5 μmol h^{-1}, respectively, which is among the top photocatalytic performance reported so far for selective photocatalytic oxidation of BA in the aqueous solution.

1. Introduction

Photocatalytic hydrogen production (PHP) is believed to be a promising technology to meet global energy demand in the near future [1–6]. Although tremendous achievements have been obtained in development of ideal photocatalytic systems, solar-driven hydrogen (H_2) production still faces many challenges for potential applications [7–12]. For instance, the use of triethanolamine (TEOA) [13], lactic acid [14] or other sacrificial reagents [15–18] might waste the energy of photogenerated holes, and introduce some valueless oxidation products and increase the cost of overall reaction process. How to realize effective consumption of the excited holes and improve PHP along with its non-carbon feature and green approach is still a big challenge.

It is known that the use of hole scavenger with a selective organic transformation is of considerable importance, as this will enhance H_2 production and the photoexcited holes simultaneously convert organic substrates into value-added chemicals [19,20]. Among various sacrificial reagents, benzyl alcohol (BA) can be employed in oxidation half reaction to meet the requirement [21–23]. The selective transformation of BA to benzaldehyde (BAD) has drawn much attention because of the fact that BAD is broadly used as important intermediates for the preparation of fragrances and pharmaceuticals in industry [24]. Traditionally, this transformation for BA oxidation is operated by hazardous stoichiometric reagents under extreme conditions such as high temperature and/or high pressure [25]. Accordingly, the photocatalytic approach for BAD synthesis by selective oxidation of BA coupled with H_2 production might be very attractive in terms of economic sustainability. The valuable products including fine chemicals and solar fuel can be simultaneously produced during photocatalytic process. The Gibbs energy (ΔG) of photocatalytic BA dehydrogenation to produce BAD and H_2 is about 28 kJ mol^{-1}, and the corresponding reaction is endergonic [26]. Researchers usually applied organic solvents including acetonitrile [27,

* Corresponding author.
** Corresponding author at: State Key Laboratory of Magnetic Resonance and Atomic and Molecular Physics, Innovation Academy for Precision Measurement Science and Technology, Chinese Academy of Sciences, Wuhan 430071, China
E-mail addresses: zhangsong@wipm.ac.cn (S. Zhang), psfwang@wit.edu.cn (F. Wang).

https://doi.org/10.1016/j.apcatb.2023.122741
Received 17 January 2023; Received in revised form 19 March 2023; Accepted 4 April 2023
Available online 5 April 2023

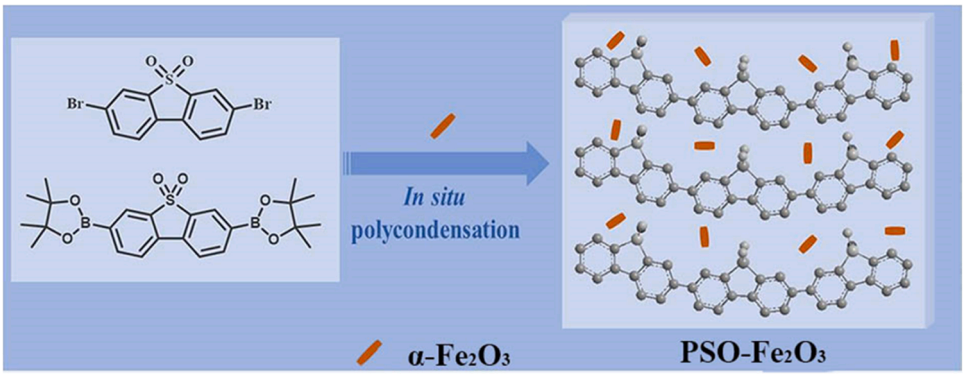

Scheme 1. Synthetic route to PSO-Fe_2O_3.

28] or benzotrifluoride [29] as a reaction media to increase the photocatalytic transformation activity of alcohols to aldehydes. However, some disadvantages, such as the potential hazard to environment and the additional cost of organic solvents, might limit their practical application in photocatalysis. Therefore, it seems great challenge to develop a novel photocatalytic system for efficient BA transformation and H_2 production in water medium.

As the novel conjugated polymers, poly(dibenzothiophene-S,S-dioxide) (PSO) and its derivative exhibit the attractive characters such as good wetting ability, high electron affinity, and rich reaction sites, which enable them to be used in artificial photocatalysis [30–34]. Nevertheless, the corresponding photocatalytic activity is hindered by the high recombination of electron−hole pairs. To enhance the separation of photoinduced charge carriers, one of the most effective methods is incorporating PSO with cost-effective inorganic semiconductor to prepare heterostructure nanocomposites. Hematite (α-Fe_2O_3), a naturally abundant and environmentally friendly oxide semiconductor, is an attractive candidate for photocatalytic water splitting due to its unique optoelectronic properties, low cost, thermodynamical stability in aqueous solution. Furthermore, α-Fe_2O_3 possesses a medium bandgap, which makes it possible to collect 40% of natural solar energy [35,36].

Conventional heterojunction inevitably leads to unfavorable losses of drive force of the photoexcited charge carriers [37]. In contrast, solid state Z-scheme hybrid photocatalyst that can effectively utilize high-energy electron and hole from semiconductor I and semiconductor II, respectively, and provide new insights for artificial photocatalysis [38,39]. Therefore, efficient Z-scheme heterojunction system is highly feasible to improve photocatalytic activity. Herein, we develop a promising strategy for the preparation of Z-scheme noble-metal-free photocatalytic system based on PSO and commercial α-Fe_2O_3 nanoparticle. To our best, this is the first time to represent conjugated polymer-Fe_2O_3 composites toward PHP coupled with selective oxidation of BA based on Z-scheme mechanism in aqueous solution. Such PSO-Fe_2O_3 composite structure can form solid Z-scheme heterojunction system that effectively promote the separation and migration of charge carries and maintain the strong reducibility and oxidizability. These synergistic advantages increased the performance for synchronous production of high value-added BAD and H_2, and the corresponding PSO-Fe_2O_3 with a mass of ~5 mg under optimal composition ratio showed an impressive photocatalytic activity with BAD and H_2 yields up to 23.1 and 29.5 μmol h^{-1}, respectively.

2. Experimental

2.1. Chemicals

α-Fe_2O_3 was provided by Shanghai Macklin Biochemical Technology Co., Ltd., BA, BAD and other reagents that we used were purchased from Aladdin Reagent Co. Ltd (Shanghai, China), and used without further purification.

2.2. Synthesis of PSO-Fe_2O_3 composites

PSO-Fe_2O_3-x were synthesized by in situ polycondensation, where x was the theoretical weight ratio between α-Fe_2O_3 nanoparticles and PSO. The synthetic route to PSO-Fe_2O_3-x is depicted in detail in supporting information.

2.3. PHP integrated with BA selective oxidation

Typically, 5 mg as-prepared photocatalyst was adequately dispersed in 50 mL BA aqueous solution. The solution was degassed using a mechanical pump at 5 ℃ and stirred for 30 min in the dark. Subsequently, H_2 production reaction coupling with photosynthesis of BAD was conducted under irradiation of a 300 W Xe lamp (PLS-SXE 300D), and the reaction was maintained at 20 ℃ by using circulating water system. The generated H_2 was detected by Labsolar-6A circulation system (Beijing Perfect light Co., Ltd) equipped with online gas chromatograph. The solution was obtained through a 0.22 μm Nylon syringe filtration and was analysed by a high-performance liquid chromatograph (HPLC) and gas chromatograph-mass spectrometry (GC-MS).

3. Results and discussion

3.1. Structure and morphology characterization

The synthetic route toward PSO-Fe_2O_3 composite is schematically illustrated in Scheme 1. The composite was prepared via Suzuki coupling reaction in the presence of α-Fe_2O_3 nanoparticles (see detailed experimental procedure in supporting information). Thermogravimetric analysis (TGA) revealed that PSO and PSO-Fe_2O_3-10 show excellent thermal stability and are suitable for PHP (Fig. S1).

Fig. S2 shows the powder X-ray diffraction (XRD) patterns of PSO, α-Fe_2O_3 and PSO-Fe_2O_3 composites. PSO is found to be a semi-crystal polymer with two characteristic peaks at 12.6° and 24.9°, which is in consistent with the reported results [30]. α-Fe_2O_3 exhibits a crystalline structure due to its sharp diffraction peaks. Upon complexation with PSO, the intensities of these characteristic peaks attributed to α-Fe_2O_3 gradually enhance with the increase of the loading amount of α-Fe_2O_3 in the composites, which suggested the formation of heterojunction of PSO-Fe_2O_3. Fourier transform infrared (FT-IR) spectroscopy of raw PSO exhibited two sharp peaks at 1302 and 1162 cm^{-1} for the stretching vibration of sulfone group (Fig. S3) [34]. The infrared-active modes of α-Fe_2O_3 in the composites were not clearly observed in the FT-IR spectrum because of the low content. However, the presence of Fe was clearly found in the in situ X-ray photoelectron spectroscopy (XPS) with binding energy of 710.9 and 724.2 eV (Fig. S4) [40]. Deconvolution of S 2p spectrum exhibited two characteristic peaks of PSO at 169.1 and

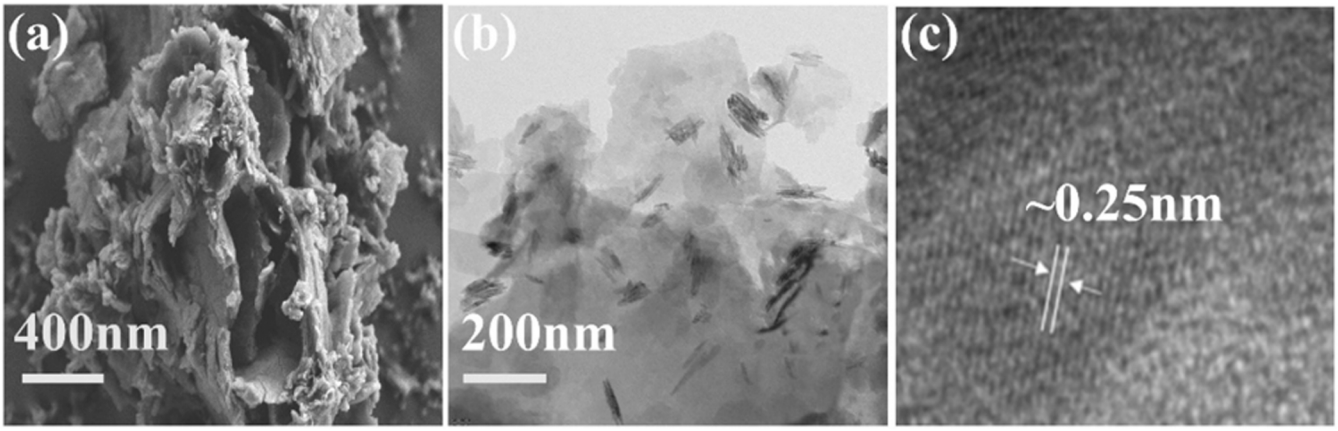

Fig. 1. (a) SEM image, (b) TEM image, (c) HRTEM image of PSO-Fe_2O_3-10.

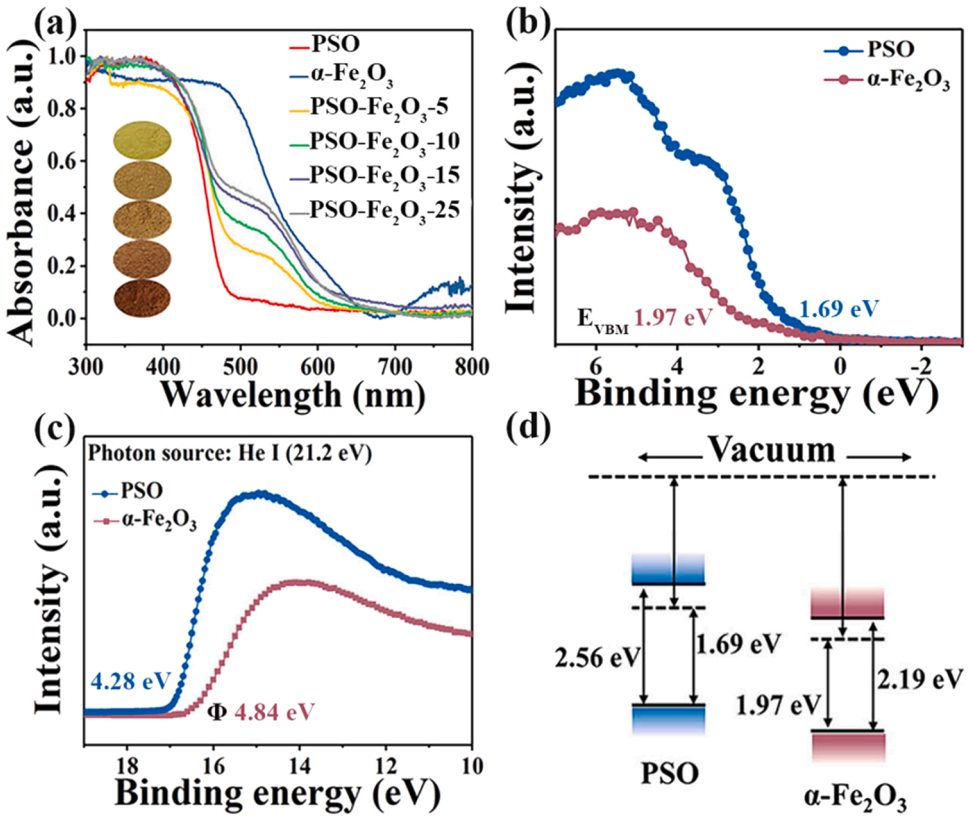

Fig. 2. (a) UV–vis DRS of PSO, α-Fe_2O_3 and PSO-Fe_2O_3 composites (inset: photographs of PSO, PSO-Fe_2O_3 composites), (b) XPS valence band spectra, (c) UPS spectra and (d) schematic of the energy level of PSO and α-Fe_2O_3.

167.9 eV. Moreover, in situ XPS measurement is a power tool to investigate the interfacial interaction between PSO and α-Fe_2O_3, which will be discussed in detail below. Field emission scanning electron microscope (SEM) was carried out to detect the nanomorphology of the as-prepared samples. As shown in Fig. 1a and Fig. S5, pure PSO consists of a sheet-like microscopic morphology, while the pristine α-Fe_2O_3 is composed of rod-like microcrystals. Comparable to that of PSO, the microscopic characteristics of PSO-Fe_2O_3 were quite similar with a wrinkled sheet nanostructure. The detailed nanomorphology structure of the corresponding composite was then investigated by HRTEM images. The lattice spacing was calculated to be approximately 0.25 nm, which is correspond to the (110) crystal plane of α-Fe_2O_3 (Fig. 1c). This result is in agreement with the observation by raw α-Fe_2O_3 (Fig. S6).

3.2. Optical properties and band structures

The optical properties of PSO, α-Fe_2O_3, PSO-Fe_2O_3 composites were studied by UV–vis diffuse reflectance spectroscopy (DRS). As shown in Fig. 2a, the absorption edges of PSO and α-Fe_2O_3 are in the range of 400−650 nm, which is prerequisite for photocatalysis in visible light region. More importantly, the as-prepared PSO-Fe_2O_3 composites exhibited a merging optical absorption ranging from 500 to 600 nm, which can be attributed to the existence of α-Fe_2O_3 phase. In addition, with the increase of the content of α-Fe_2O_3, the optical absorption of PSO-Fe_2O_3 composites is gradually enhanced, which is in line with its gradual deepening color (inset of Fig. 2a). The optical bandgap of PSO and α-Fe_2O_3 was calculated to be 2.56 and 2.19 eV by the Tauc plot,

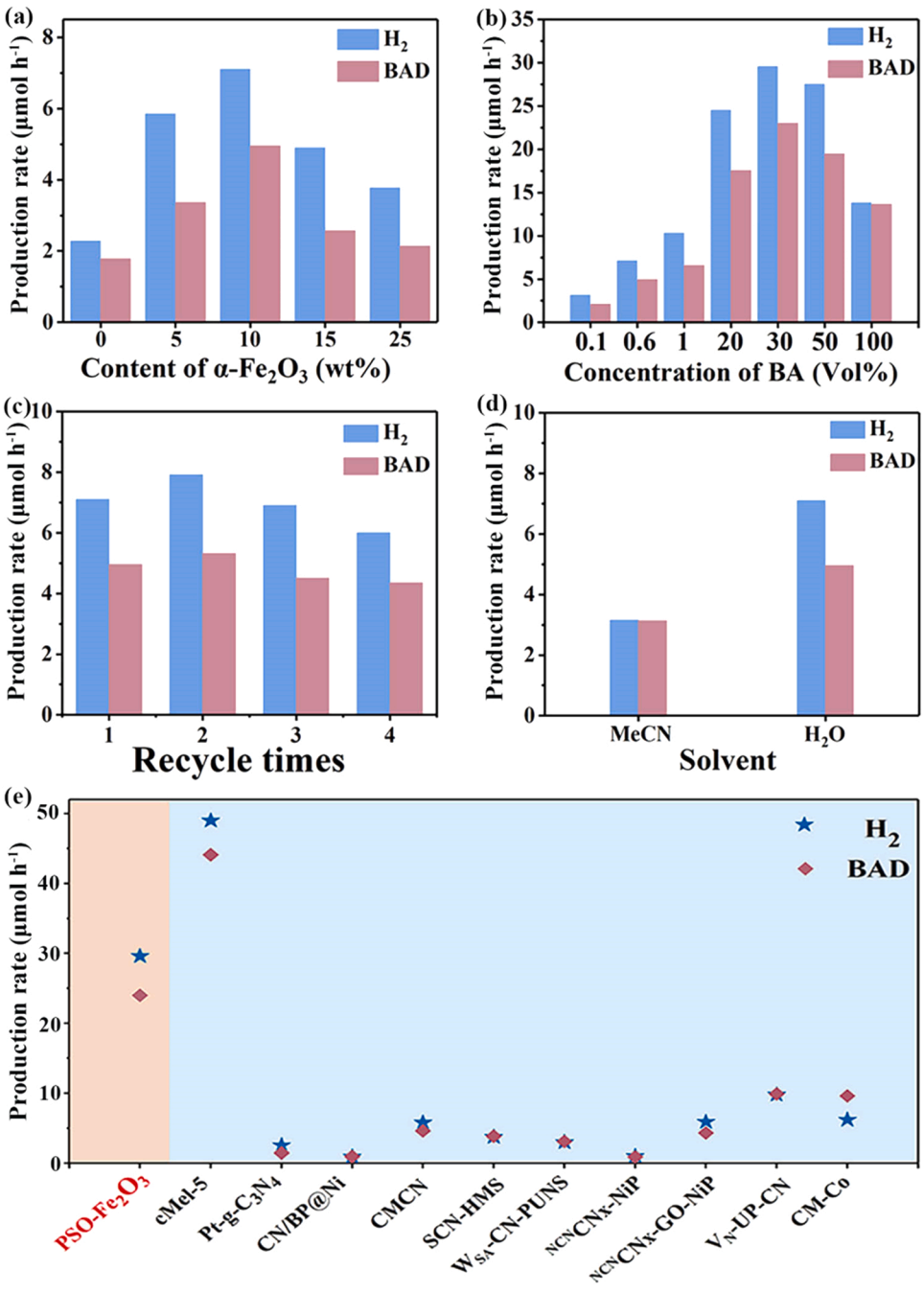

Fig. 3. H_2 evolution coupled with selective oxidation of BA (a) with PSO and PSO-Fe_2O_3 composites in BA (0.6 vol%) aqueous solution, (b) with PSO-Fe_2O_3-10 under different BA concentration, (c) recycling tests of PSO-Fe_2O_3-10 in BA (0.6 vol%) aqueous solution, (d) with PSO-Fe_2O_3-10 in different BA (0.6 vol%) solution (acetonitrile or water as solvent), experimental condition: 5 mg photocatalysts, 50 mL BA aqueous solution, UV–vis light. (e) H_2 and BAD evolution for PSO-Fe_2O_3-10 in comparison with representative photocatalysts. The concrete test details are described in Table S1.

respectively (Fig. S7).

To further determine the energy band positions of PSO and α-Fe_2O_3, the valence band (VB) and work function were calculated by XPS spectroscopy and ultraviolet photoemission spectroscopy (UPS), respectively. According to the XPS measurement (Fig. S8), the VB maximum positions (E_{VBM}) of PSO and α-Fe_2O_3 were estimated to be 1.69 and 1.97 eV (vs Fermi level, E_f), respectively (Fig. 2b). The work function of PSO and α-Fe_2O_3 were calculated respectively to be 4.28 and 4.84 eV (Fig. 2c and Fig. S9). The work function represents the energy of E_f relative to vacuum level [41]. Therefore, the E_f of PSO and α-Fe_2O_3 were −4.28 and −4.84 eV, respectively. The results show that PSO and α-Fe_2O_3 are reduction photocatalyst and oxidation photocatalyst, respectively. And there is electron transfer at the interface area due to the difference of E_f between PSO and α-Fe_2O_3 [42]. A schematic graph of energy band locations is illustrated in Fig. 2d and Fig. S10.

3.3. Photocatalytic activity in BA aqueous solution

To evaluate the photocatalytic performance of as-prepared samples, H_2 production reaction coupling with photosynthesis of BAD was carried out in BA aqueous solution under UV–vis light irradiation for 4 h at 20 ℃. As shown in Fig. 3a, the pure PSO exhibited low efficiency for production of H_2 and BAD, while the photocatalytic activity was significantly enhanced with the increased concentration of BA (Fig. S11). The possible reason is that the photogenerated holes could be effectively consumed by BA molecules during the photocatalytic process, leading to more efficient charge transfer and separation. Upon complexation with α-Fe_2O_3, the photocatalytic performance was remarkable improved, demonstrating that α-Fe_2O_3 has a key role for H_2 production with splitting of BA. Both H_2 production rate and BAD yield initially enhanced with increasing the concentration of α-Fe_2O_3. The

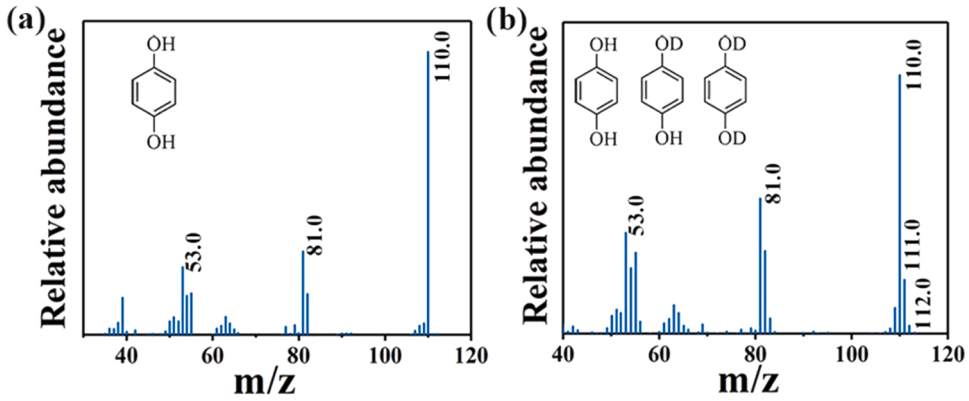

Fig. 4. MS spectra of (a) 1,4-hydroquinone standard substance and (b) 1,4-hydroquinone deuterated compound. Experimental condition: 5 mg PSO-Fe_2O_3-10, 50 mL BA (0.6 vol%) aqueous solution or D_2O solution, 1 mg BQ.

composition-optimized PSO-Fe_2O_3-10 exhibited an impressive H_2 evolution rate of 7.5 μmol h^{-1} and a simultaneous BAD generation rate of 5.0 μmol h^{-1}. Meanwhile, the selectivity for the synthesis of BAD was high as 96% after 4 h of light illumination in UV–vis region (Fig. S12a). Further increasing the ratio of α-Fe_2O_3 to PSO lead to a decrease of the photocatalytic performance. The possible reason is that self-aggregated α-Fe_2O_3 could reduce the density of heterojunctions in PSO-Fe_2O_3 composites. While with the content of α-Fe_2O_3 being lower the optimal ratio, the corresponding composite might not contain enough α-Fe_2O_3 nanoparticles to transfer the photogenerated carriers, resulting in lower separation efficiency of electron–hole pairs [43]. Residual Pd in PSO--Fe_2O_3-10 would be used as a cocatalyst for promote the photocatalytic performance [44]. The residual Pd content was 0.03 wt% measured by ICP-MS. Thus, the trace residual Pd had negligible influence on the photocatalytic activity.

The photocatalytic performance of PSO-Fe_2O_3-10 for H_2 and BAD production was investigated under different BA concentration. In the beginning, the photocatalytic activity of PSO-Fe_2O_3-10 was significantly improved with an increasing amount of BA. These results suggest that the concentration of BA play an important role on the production of H_2 and BAD. BA as an electron donor can effectively scavenge photogenerated holes, thus greatly promoting photocatalytic H_2 production from water splitting and the dehydrogenation of BA, which would be demonstrated by isotope labelling method in this study. Specifically, when the concentration of BA was 30 vol%, the maximum amount of H_2 (29.5 μmol h^{-1}) and BAD (23.1 μmol h^{-1}) were simultaneously obtained from PSO-Fe_2O_3-10 with a mass of ~5 mg in 50 mL aqueous solution after 4 h of light irradiation (Fig. 3b). To our best, this is among the top photocatalytic performance by using organic-inorganic composites for H_2 production coupled with selective oxidation of BA in aqueous solution reported to date (Fig. 3e). However, when the concentration is higher than 30 vol%, the production of BAD obviously reduces to 19.5 μmol h^{-1}. It may be owing to that excess BA was adsorbed on the surface of PSO-Fe_2O_3-10, which could slow down the desorption process of BAD and suppress selective oxidation of BA. In addition, the poor solubility of BA in water is the limiting factor for better photocatalytic performance at high BA concentration. We noted that high concentration of BA would cause the aggregation of the photocatalyst PSO-Fe_2O_3-10 and reduce the dispersity of PSO-Fe_2O_3-10 in BA aqueous solution. DLS measurement demonstrated that the particle size of PSO-Fe_2O_3-10 increases with the increase of BA concentration (Fig. S13). As a result, the particle-aggregation may cause the decreased utilization ratio of reaction sites for the activation of BA. Therefore, the photocatalytic performance of PSO-Fe_2O_3-10 decrease when the concentration of BA is higher than 30 vol%. When pure BA was conducted, H_2 and BAD generation were measured to be 13.8 and 13.6 μmol h^{-1}, respectively, and the ratio of BAD to H_2 production was ~1:1. The result suggested that BA was consumed to produce H_2 and BAD through the light-driven alcohol splitting reaction. Comparatively, no H_2 and O_2 can be detected under photocatalysis of PSO-Fe_2O_3-10 in 3 h without adding BA in pure water due to the rapid recombination of excited holes and electrons (Fig. S14). BA was used as the electron donor, which could react irreversibly with the photogenerated holes and promote H_2 production. Therefore, it was of more attractive to combine H_2 production coupled with selective oxidation of BA.

The recyclability and stability of PSO-Fe_2O_3-10 under the optimal condition was evaluated. As shown in Fig. 3c and Fig. S12b, the photocatalytic performance of PSO-Fe_2O_3-10 did not exhibit obvious decrease in BA aqueous solution after four cycles of test, suggesting the moderate reusability and photostability of the resulting photocatalyst. In addition, no significant change could be observed in XRD (Fig. S15), FT-IR (Fig. S16), UV−vis DRS (Fig. S17), PL (Fig. S18), SEM (Fig. S19) measurements after photocatalysis, which suggested that the structure of PSO-Fe_2O_3-10 might remain basically stable after long-term irradiation. Apparent quantum yield (AQY) of PSO-Fe_2O_3-10 for H_2 production was further measured under optimal condition with the concentration of BA (30 vol%). As shown in Fig. S20, a maximum AQY was 5.2% at 365 nm, which show a moderate quantum efficiency compared to that of other photocatalysts. The AQY value decreased to 1.83%, 0.74% and 0.37% at 420, 475, and 550 nm, respectively, which might be attributed to the weak adsorption of PSO-Fe_2O_3-10 at the given wavelengths.

Previous studies revealed that carbonyl compounds might be decomposed by reactive oxygen species, especially for nonselective hydroxyl radicals (•OH). Thus, acetonitrile was used as a reaction media in the conventional strategy, which can efficiently reduce the production of •OH and retain the preferential selectivity toward BAD [24]. To investigate the effect of the reaction media on the photocatalytic activity, BA oxidation in acetonitrile solution over PSO-Fe_2O_3-10 was conducted under the same condition. Interestingly, when comparing the BA transformation efficiency of PSO-Fe_2O_3-10 in acetonitrile and aqueous media, it was observed that the photocatalytic system exhibited much higher performance in green aqueous solution than that in acetonitrile (Fig. 4d). This could be attributed to competition between acetonitrile molecules and BA molecules, where acetonitrile molecules might be adsorbed on the surface of PSO-Fe_2O_3-10 and constrain the BA absorption to give skimpy proton concentration, which served as the exclusive proton source. Thus, water was preferred as the green media for selective dehydrogenation of BA and H_2 production over PSO--Fe_2O_3-10. The possible reason is that water might have acted as the source for hydrogen protons, resulting in an increase of reaction sites.

3.4. H_2 source verification

As mentioned above, the yields of H_2 and BAD were 13.8 and 13.7 μmol h^{-1} in 100 vol% BA solution, respectively, suggesting that BA molecules was utilized to generate BAD and H_2. In other words, BA

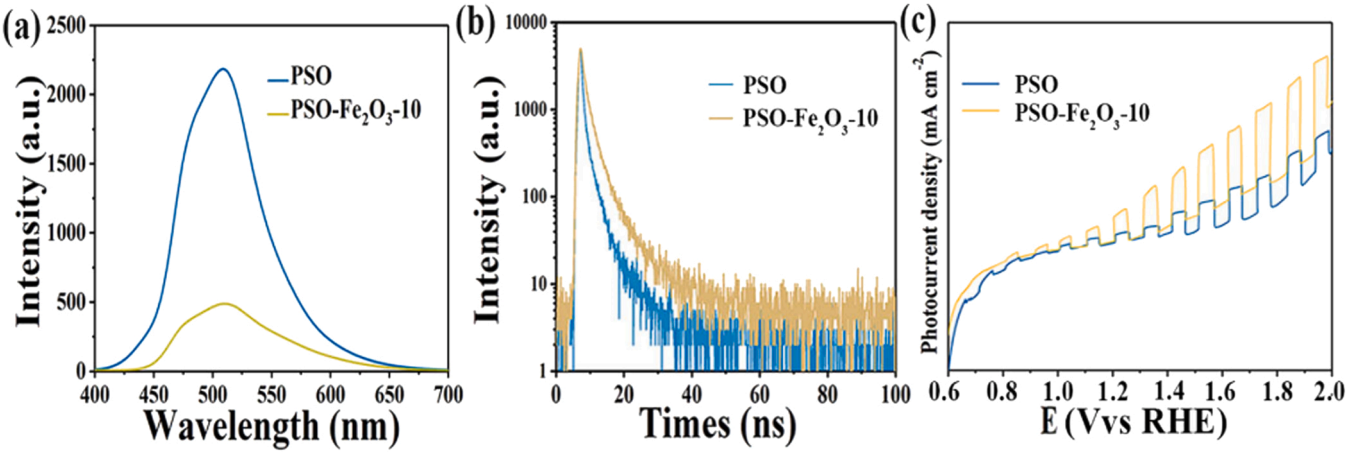

Fig. 5. (a) PL spectra, (b) time-resolved PL decay curves and (c) photocurrent density−potential under chopped light of PSO and PSO-Fe_2O_3-10.

provides the source of hydrogen protons. To further clarify the H_2 source in BA aqueous solution during photocatalysis, the control photocatalytic experiment with 1,4-benzoquionone (BQ) as $\bullet O_2^-$ scavenger was carried out. The reaction mixture was extracted with ethyl acetate and the BQ reduction products were identified by mass spectrometer. It was observed that the 1,4-hydroquinone, a reduction product of BQ, was

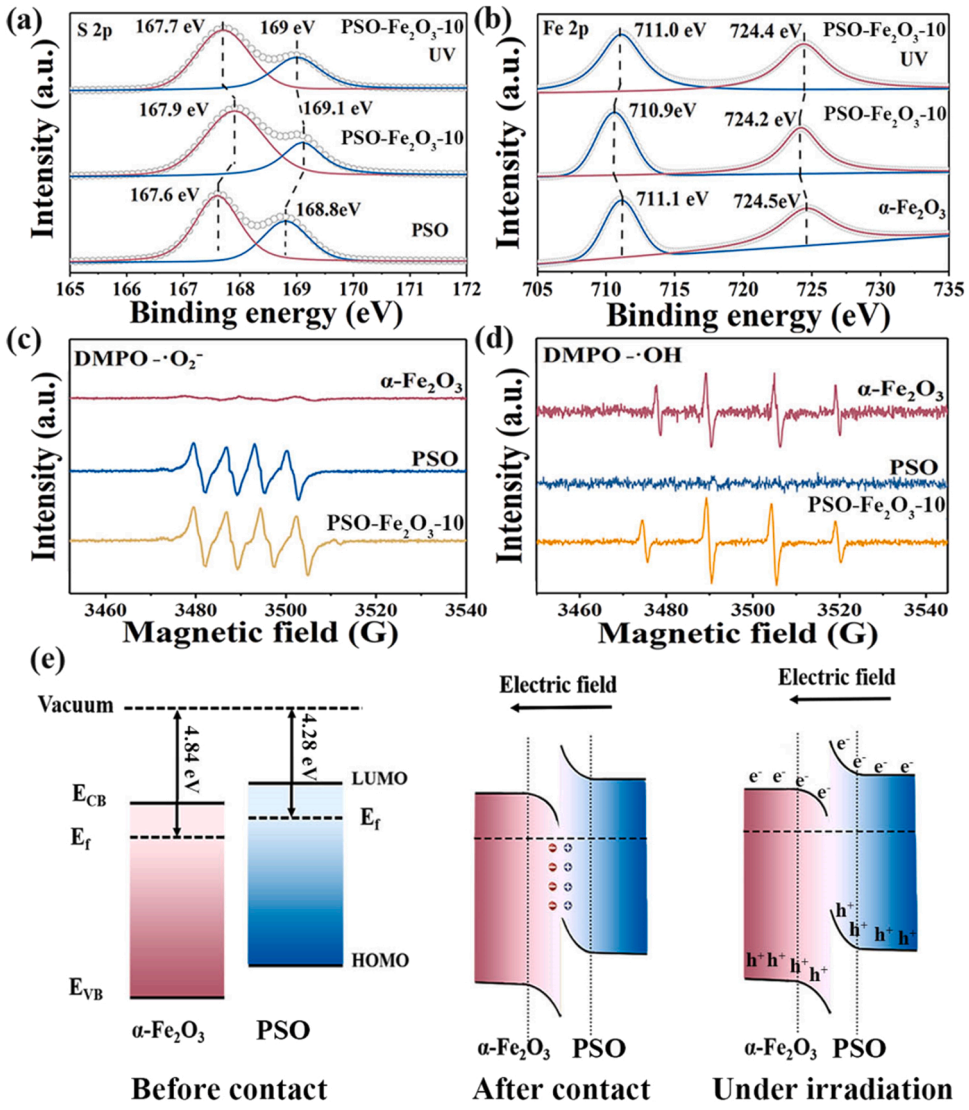

Fig. 6. High-resolution XPS spectra of (a) S 2p, (b) Fe 2p, EPR spectra of (c) DMPO-$\bullet O_2^-$ and (d) DMPO-$\bullet$OH over α-Fe_2O_3, PSO and PSO-Fe_2O_3-10 under light illumination, (e) schematic illustration of charge transfer process for Z-scheme heterojunction.

detected with the molecular ion peak of $m/z = 110$ in the BA system (Fig. 4a). When deuterium oxide was used instead of water as solvent, the molecular ion peak of the reduction product of BQ in deuterium oxide solution is $m/z = 111$ (Fig. 4b and Fig. S21). These results demonstrated that deuterated 1,4-hydroquinone was existed in the BQ reduction products. Therefore, we might conclude that the protons derived from water and BA were reduced to PHP in aqueous solution [45].

3.5. Effect of various sacrificial agents for PHP

Considering the heterostructure and good optoelectronic properties of PSO-Fe_2O_3-10, we were also interested in assessing the PHP performance with the three widely used sacrificial agents such as triethylamine (TEA)/MeOH, TEOA and ascorbic acid (AA). As shown in Fig. S22−24, the photocatalytic activity of pure PSO was less than that of PSO-Fe_2O_3-10, which further demonstrated that α-Fe_2O_3 played a key role in charge carrier transfer and separation. Moreover, PSO-Fe_2O_3-10 with a mass of 5 mg exhibited the highest photocatalytic activity with hydrogen evolution rate of 295.4 μmol h^{-1} in the presence of TEOA (Fig. S22). In contrast, the PHP performance of PSO-Fe_2O_3-10 was obviously decreased under the identical conditions when the sacrificial agent was AA or TEA/MeOH. This indicated that TEOA adsorbed on the surface of PSO-Fe_2O_3-10 can easily react with the photogenerated holes (or •OH) to decrease the charge recombination, leading to the enhancement of hydrogen production efficiency [46].

3.6. Wetting ability of photocatalyst

The surface hydrophilicity of PSO, α-Fe_2O_3, and PSO-Fe_2O_3 composites was evaluated by using their contact angles (CA). As shown in Fig. S25, raw polymer PSO showed the best hydrophilic surface with a CA of 38.1°. Once complexation with α-Fe_2O_3, the CAs increased to 38.6°, 46.9°, 55.6°, and 65.2° for PSO-Fe_2O_3-5, PSO-Fe_2O_3-10, PSO-Fe_2O_3-15 and PSO-Fe_2O_3-25, respectively, suggesting that the wetting ability of PSO-Fe_2O_3 was decreased as the increased amount of α-Fe_2O_3 in the composites. PSO-Fe_2O_3-10 shows a moderate hydrophilic surface among the prepared composites, while it exhibits the best photocatalytic activity towards selective oxidation of BA with synchronous H_2 production. Therefore, we might conclude that the wetting properties play a role but are not a key factor in the photocatalytic activities of PSO-Fe_2O_3 composite.

3.7. The charge transfer efficiency of PSO-Fe_2O_3

To explore the separation efficiency of photoexcited electron–hole pairs, steady-state photoluminescence (PL) measurement of as-prepared photocatalysts has been conducted. PL emission originate from the radiative recombination between holes and electrons. Thus, the PL peak intensity is proportional to the extent of radiative recombination, that is, lower is the intensity, the lower is the recombination rate. Compared with raw PSO, the intensity of PSO-Fe_2O_3-10 is obviously decreased at 520 nm (Fig. 5a), suggesting rapid charge transfer, which suppressed electron−hole recombination [47]. In addition, the recombination kinetics of charge carriers was investigated by time-resolved fluorescence spectroscopy. PSO-Fe_2O_3-10 exhibited a longer average fluorescence lifetime of 2.82 ns (Fig. 5b and Table S3). The possible reason is that PSO constructs a heterostructure with α-Fe_2O_3, which is beneficial to interface charge transfer and separation, and prolong the lifetime of generated electron−hole pair [48].

Photocurrent density was employed in three-electrode system to evaluate the charge generation and migration efficiency of PSO-Fe_2O_3-10. The photocurrent density−potential under chopped light was measured using linear sweeping voltammetry (LSV) curves. As shown in Fig. 5c, PSO-Fe_2O_3-10 show higher photocurrent density than raw PSO under light illumination, which indicated that PSO-Fe_2O_3-10 heterojunction has stronger response to light and generate more photoelectrons. Photocurrent response−time have been investigated at 0.6 V vs RHE under light on/off for further understand the photocurrent response of PSO-Fe_2O_3-10 (Fig. S26). The photocurrent density of PSO-Fe_2O_3-10 and PSO rise rapidly while light on and turn back quickly while light off. More importantly, PSO-Fe_2O_3-10 possess maximum photocurrent density under light on, which is consistent with the Fig. 5c, further demonstrating that PSO-Fe_2O_3-10 is beneficial to photogenerated electron transfer.

3.8. Mechanism of photogenerated charge carrier transfer

In order to further investigated the interfacial interaction between PSO and α-Fe_2O_3, the photo-electrons migration of PSO-Fe_2O_3 composite was monitored using in situ XPS measurement. As show in Fig. 6a, b and Fig. S27, upon complexing PSO with α-Fe_2O_3, the binding energy of S 2p in PSO-Fe_2O_3-10 display a positive shift to 169.1 and 167.9 eV, while the binding energy of Fe 2p shift negatively to 710.9 and 724.2 eV. Generally, the shifts illustrate a strong interaction between PSO and α-Fe_2O_3, and a built-in electric field were formed at the PSO-Fe_2O_3 interface. Additionally, when in situ XPS measurement was performed under light irradiation, the peaks of Fe 2p shift positively and the peaks of S 2p shift negatively, which demonstrated the photogenerated electrons transferred from α-Fe_2O_3 to PSO [49].

To clarify the mechanism of PSO-Fe_2O_3 composite, electron paramagnetic resonance (EPR) was conducted to monitor the transient radical species of •OH and $\bullet O_2^-$ by using 5,5-dimethyl-1-pyrroline-N-oxide (DMPO) as a trapping agent. As shown in Fig. 6c, PSO and PSO-Fe_2O_3-10 exhibited stronger DMPO− $\bullet O_2^-$ signals with relative intensity of 1:1:1:1 under light irradiation, whereas no peak was detected in the EPR spectrum of α-Fe_2O_3. On the other hand, it can be observed that the typical DMPO− •OH signals were seen for PSO-Fe_2O_3-10 and α-Fe_2O_3 (Fig. 6d). However, no apparent EPR peaks were observed in the dark (Fig. S28), suggesting that photocatalytic process is indeed dependent on light illumination. As shown in Fig. S29, CB potentials are −1.09 and 0.12 V, and VB potentials are 1.47 and 2.31 V (vs NHE) for PSO and α-Fe_2O_3, respectively. However, the reduction potential of $O_2/\bullet O_2^-$ is −0.33 V and the oxidation potential of $OH^-/\bullet OH$ is 1.99 V under standard condition [50]. According to the traditional type II heterojunction principle, photoexcited holes migrate from α-Fe_2O_3 to PSO with a more negative VB, and photogenerated electrons transfer from PSO to α-Fe_2O_3 with a more positive CB. The drive forces for hole oxidation of PSO and electron reduction of α-Fe_2O_3 are not enough to generate •OH and $\bullet O_2^-$, respectively. However, PSO-Fe_2O_3-10 could maintain the strong reductive ability of raw PSO and oxidative ability of the pristine α-Fe_2O_3. Therefore, the Z-scheme charge transfer in PSO-Fe_2O_3 composite was confirmed.

Fig. 6e exhibits charge transfer and separation mechanism of the Z-scheme PSO-Fe_2O_3 heterojunction. When α-Fe_2O_3 contacted with PSO intimately, electrons within PSO spontaneously migrated to α-Fe_2O_3 via interfaces until their E_f was equal. α-Fe_2O_3 obtained the electrons and was negatively charged, while PSO lose electrons and was positively charged at the interface. Thus, a robust built-in electron field was established, directing from PSO to α-Fe_2O_3. Under light irradiation, the photoexcited electrons will be jumped from VB to CB. Some photoelectrons from CB of α-Fe_2O_3 might combine holes from VB of PSO due to the internal electric field and band edge bending effect at the interface. At the same time, the photoexcited electrons in the CB of PSO and holes in the VB of α-Fe_2O_3 will be maintained. Therefore, the Z-scheme charge transfer mechanism is testified for PSO-Fe_2O_3 heterojunction, which not only boost the separation efficiency of photogenerated electron−hole pairs, but also possesses maximized capacity for BA oxidation and H_2 production.

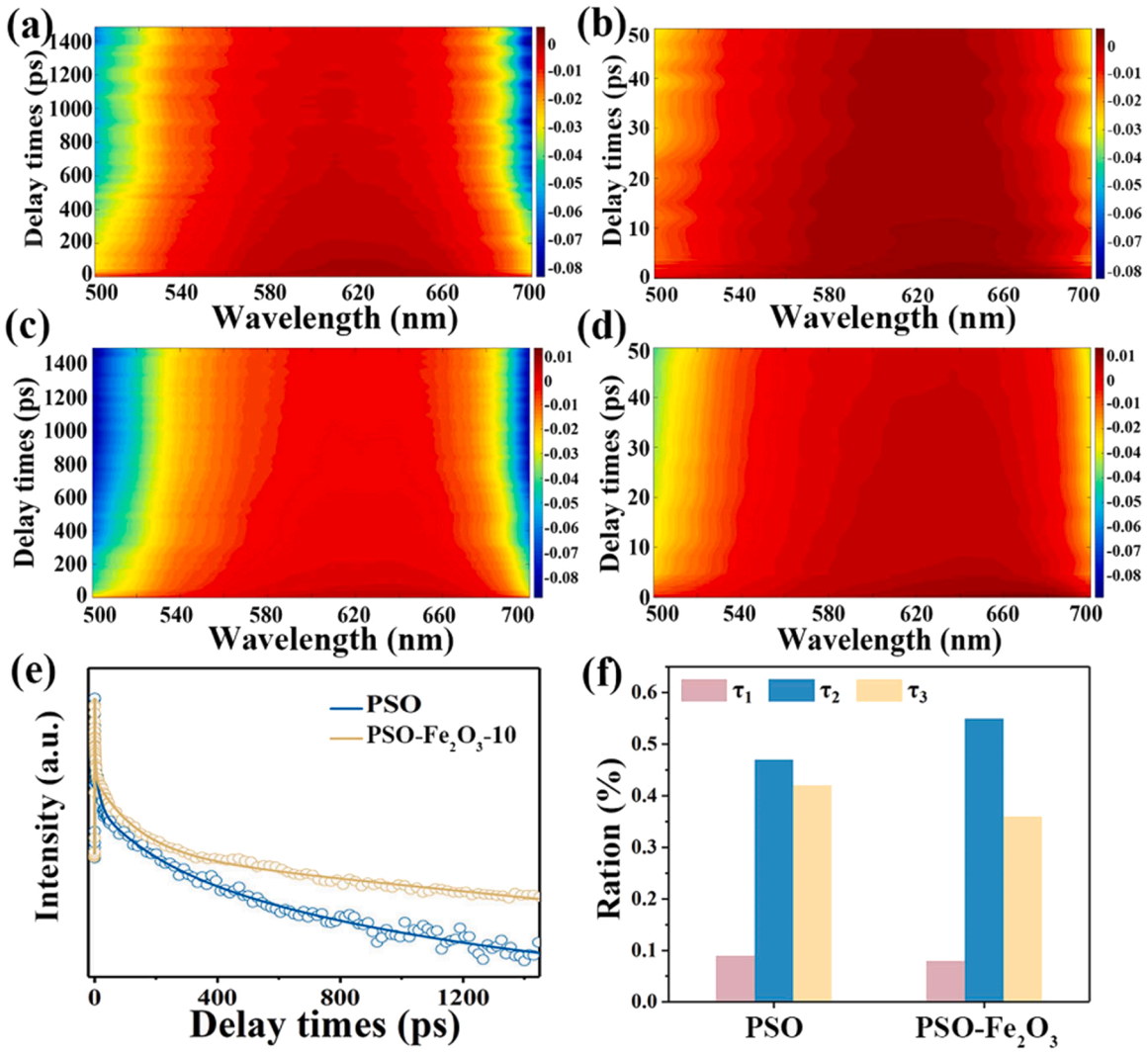

Fig. 7. Two-dimensional TAS of PSO and PSO-Fe_2O_3-10 in acetonitrile. Delay times of PSO up to (a) 1400 ps and (b) 50 ps, delay times of PSO-Fe_2O_3-10 up to (c) 1400 ps and (d) 50 ps; the color intensity reflects signal magnitude. (e) Time profiles of normalized transient absorption at selected 620 nm, (f) weights of lifetime components for PSO and PSO-Fe_2O_3-10 after 400 nm laser irradiation.

Table 1
The global fit analysis of the absorption-time profiles of PSO and PSO-Fe_2O_3-10.

Sample	a_1 [%]	τ_1 [ps]	a_2 [%]	τ_2 [ps]	a_3 [%]	τ_3
PSO	9	4.4	47	318	42	ns
PSO-Fe_2O_3-10	8	3.1	55	248	36	ns

3.9. Transient spectroscopy

Transient absorption spectroscopy (TAS) was used to investigate the charge transportation dynamics of PSO-Fe_2O_3 heterojunction on the picosecond timescale. Fig. 7a–d shows the contour plots of the pump-induced absorption change (ΔOD) spectra as a function of delay time for PSO and PSO-Fe_2O_3-10. Both TAS spectra exhibit broadband signals from 550 nm to 680 nm, which is assigned to the excited state absorption. These spectral features show relatively slow charge carrier kinetics and remain in a long delay time. For pure α-Fe_2O_3 sample, the transient absorption decayed more rapidly, suggesting that the kinetics of electron–hole recombination occurred on shorter timescales in the photocatalytic monosystem (Fig. S30).

To clarify the charge carrier dynamics, a global fit analysis on 2D data matrix was recorded for PSO and PSO-Fe_2O_3-10 with a singular value decomposition (Fig. S31). The decay transients are well described by a triexponential fitting function. The fitting results yielded three decay components τ_1, τ_2 and τ_3 with different time constants and component proportions, as listed in Table 1. And time profiles of transient absorption of PSO and PSO-Fe_2O_3-10 at selected wavelength (620 nm) are shown in Fig. 7e. The time constants of the triexponential components were obtained to be 4.4 ps, 318 ps, and ns scale in PSO, respectively, which is in good agreement with the previous results [31]. The several and hundreds ps components can be attributed to electron diffusion and trapping processes in PSO, respectively. The longest ns component is assigned to the recombination of non-geminate charge carriers. After hybridization PSO with α-Fe_2O_3, the heterostructure dynamics showed faster excited electron diffusion process in comparison with that of raw PSO, which suggests an additional decay pathway in the presence of α-Fe_2O_3. The possible reason is that the band bending at the heterojunction interface induces a built-in field, promoting the migration of electrons between PSO and α-Fe_2O_3. The lifetime required for electron diffusion is proved to be in several ps, which is reasonably consistent with the first τ_1 component [51]. The component with shorter lifetime of τ_2 (248 ps) is primarily originated from electrons trapping processes within PSO-Fe_2O_3-10 heterojunction. Furthermore, it is noticed that the weight of the component of electronic trapping in PSO-Fe_2O_3-10 achieves at 55% ratio and is noticeably higher than that

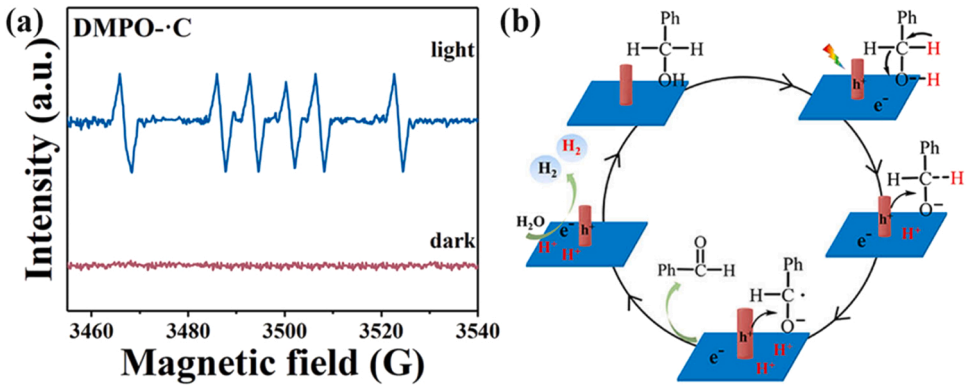

Fig. 8. (a) EPR spectra of carbon-centered radical over PSO-Fe_2O_3-10 under light illumination using DMPO as the trapping reagent, (b) proposed potential mechanism of the photocatalytic BA splitting in aqueous solution over PSO-Fe_2O_3-10.

in PSO (Fig. 7f). It illustrates that a more efficient and faster electron transfer occur in PSO-Fe_2O_3-10. Therefore, the timely charge separation as well as the rapid electron trapping accounted for the suppressed charge recombination and supported the heterojunction formation between PSO and α-Fe_2O_3.

3.10. Mechanism of photocatalytic reaction in BA aqueous solution

EPR spectroscopic technique using DMPO as the trapping reagent was employed to monitor the reaction to evaluate the radical intermediate. As presented in Fig. 8a, six signal peaks for carbon-centered radical can be clearly observed under 300 W Xe lamp irradiation. However, there was no EPR signal in the presence of DMPO without illumination, suggesting that the formation of carbon-centered free radicals was triggered by light driven photosynthesis [52]. According to the experiment results mentioned above, a possible mechanism toward the H_2 generation coupled with BA oxidation over PSO-Fe_2O_3 was proposed. On the basis of Z-scheme principle, the electrons in the CB of α-Fe_2O_3 rapidly recombine with the holes in the VB of PSO via the internal electronic field under light irradiation. Therefore, many reductive electrons would accumulate in the CB of PSO while a large number of oxidative holes concentrate in the VB of α-Fe_2O_3. As illustrated in Fig. 8b, an active BA molecule on the surface of photocatalysts was deprotonated to generate one alkoxide anion and a H^+ from hydroxyl group. Subsequently, the photogenerated hole from VB of α-Fe_2O_3 reacted with the alkoxide anion, resulting in one corresponding carbon radical and proton during this photocatalysis process. Finally, carbon-centered radical was further oxidized to form BAD, and the two protons or water reacted with electrons to release H_2 molecule simultaneously.

4. Conclusions

In summary, a series of PSO-Fe_2O_3 heterojunction photocatalysts were rationally designed and synthesized via in situ polymerization, and could be employed as actively dual-functional materials toward photooxidation of BA coupled with H_2 production. PL, XPS, EPR and TAS were applied for characterization, and the results suggested that the Z-scheme heterojunction PSO-Fe_2O_3 exhibited close contact at the interface, which can effectively increase charge transfer and separation, and maintain the robust reducibility of PSO and oxidizability of α-Fe_2O_3 simultaneously, ultimately enhance photocatalytic performance. At the optimal α-Fe_2O_3 content, the resulting composite PSO-Fe_2O_3-10 with a mass of ~5 mg showed the highest photocatalytic activity with an impressive H_2 and BAD evolution rate of 29.5 and 23.1 μmol h^{-1}, respectively. In addition, PSO-Fe_2O_3 composite possess a higher efficiency in aqueous solution in comparison to the corresponding acetonitrile media for light-driven BAD transformation. Remarkably, photocatalytic BA oxidation coupled with H_2 production over polymer-based photocatalysts in aqueous solution is still rare. Thus, this study might provide the feasibility of Z-scheme heterojunction photocatalysts for selective BA oxidation coupled with H_2 in the green media.

CRediT authorship contribution statement

Jun Wu: Investigation, Methodology, Formal analysis, Data curation, Writing – original draft. **Ye Wang**: transient spectroscopy testing, Data curation. **Song Zhang**: transient spectroscopy analysis, Data curation. **Yuxiang Liu**: Data curation. **Feng Wang**: Supervision, Writing –review & editing. All authors contributed to finalizing the manuscript.

Declaration of Competing Interest

The authors declare that they have no known competing financial interests or personal relationships that could have appeared to influence the work reported in this paper.

Data Availability

The data that has been used is confidential.

Acknowledgements

This work was financially supported by Educational Commission of Hubei Province of China (D20181505), the National Key Research and Development Program of China (No. 2019YFA0307700), the National Natural Science Foundation of China (Nos. 22273116, 12274418, 11974381) and the Knowledge Innovation Program of Wuhan-Basic Research (No. S22H210301).

Appendix A. Supporting information

Supplementary data associated with this article can be found in the online version at doi:10.1016/j.apcatb.2023.122741.

References

[1] K.P. Sokol, W.E. Robinson, J. Warnan, N. Kornienko, M.M. Nowaczyk, A. Ruff, J. Z. Zhang, E. Reisner, Bias-free photoelectrochemical water splitting with photosystem II on a dye-sensitized photoanode wired to hydrogenase, Nat. Energy 3 (2018) 944–951, https://doi.org/10.1038/s41560-018-0232-y.
[2] C. Yang, B.C. Ma, L.Z. Zhang, S. Lin, S. Ghasimi, K. Landfester, K.A.I. Zhang, X. C. Wang, Molecular engineering of conjugated polybenzothiadiazoles for enhanced hydrogen production by photosynthesis, Angew. Chem. Int. Ed. 55 (2016) 9202–9206, https://doi.org/10.1002/anie.201603532.
[3] Y. Bai, L. Wilbraham, H. Gao, R. Clowes, H.F. Yang, M.A. Zwijnenburg, A.I. Cooper, R.S. Sprick, Photocatalytic polymers of intrinsic microporosity for hydrogen

production from water, J. Mater. Chem. A 9 (2021) 19958–19964, https://doi.org/10.1039/d1ta03098a.
[4] X.B. Chen, S.H. Shen, L.J. Guo, S.S. Mao, Semiconductor-based photocatalytic hydrogen generation, Chem. Rev. 110 (2010) 6503–6570, https://doi.org/10.1021/cr1001645.
[5] J.H. Kim, D. Hansora, P. Sharma, J.W. Jang, J.S. Lee, Toward practical solar hydrogen production an artificial photosynthetic leaf-to-farm challenge, Chem. Soc. Rev. 48 (2019) 1908–1971, https://doi.org/10.1039/c8cs00699g.
[6] H. Nishiyama, T. Yamada, M. Nakabayashi, Y. Maehara, M. Yamaguchi, Y. Kuromiya, Y. Nagatsuma, H. Tokudome, S. Akiyama, T. Watanabe, R. Narushima, S. Okunaka, N. Shibata, T. Takata, T. Hisatomi, K. Domen, Photocatalytic solar hydrogen production from water on a 100-m^2 scale, Nature 598 (2021) 304–307, https://doi.org/10.1038/s41586-021-03907-3.
[7] C.Z. Han, S.H. Xiang, M.T. Ge, P.X. Xie, C. Zhang, J.X. Jiang, An efficient electron donor for conjugated microporous polymer photocatalysts with high photocatalytic hydrogen evolution activity, Small 18 (2022) 2202072, https://doi.org/10.1002/smll.202202072.
[8] J.L. Wang, G.C. Ouyang, Y. Wang, X.L. Qiao, W.S. Li, H.X. Li, 1,3,5-triazine and dibenzo[b,d] thiophene sulfone based conjugated porous polymers for highly efficient photocatalytic hydrogen evolution, Chem. Commun. 56 (2020) 1601–1604, https://doi.org/10.1039/c9cc08412f.
[9] R.S. Sprick, B. Bonillo, R. Clowes, P. Guiglion, N.J. Brownbill, B.J. Slater, F. Blanc, M.A. Zwijnenburg, D.J. Adams, A.I. Cooper, Visible-light-driven hydrogen evolution using planarized conjugated polymer photocatalysts, Angew. Chem. Int. Ed. 55 (2016) 1824–1828, https://doi.org/10.1002/anie.201510542.
[10] D. Schwarz, Y.S. Kochergin, A. Acharjya, A. Ichangi, M.V. Opanasenko, J. Cejka, U. Lappan, P. Arki, J.J. He, J. Schmidt, P. Nachtigall, A. Thomas, J. Tarabek, M. J. Bojdys, Tailored band gaps in sulfur- and nitrogen-containing porous donor-acceptor polymers, Chem. Eur. J. 23 (2017) 13023–13027, https://doi.org/10.1002/chem.201703332.
[11] P. Kuhn, M. Antonietti, A. Thomas, Porous, covalent triazine-based frameworks prepared by ionothermal synthesis, Angew. Chem. Int. Ed. 47 (2008) 3450–3453, https://doi.org/10.1002/anie.200705710.
[12] T. Banerjee, F. Haase, G. Savasci, K. Gottschling, C. Ochsenfeld, B.V. Lotsch, Single-site photocatalytic H_2 evolution from covalent organic frameworks with molecular cobaloxime Co-Catalysts, J. Am. Chem. Soc. 139 (2017) 16228–16234, https://doi.org/10.1021/jacs.7b07489.
[13] Y.G. Xiang, X.P. Wang, X.H. Zhang, H.J. Hou, K. Dai, Q.Y. Huang, H. Chen, Enhanced visible light photocatalytic activity of TiO_2 assisted by organic semiconductors: a structure optimization strategy of conjugated polymers, J. Mater. Chem. A 6 (2018) 153–159, https://doi.org/10.1039/c7ta09374h.
[14] Z.P. Li, W.X. Huang, J.X. Liu, K.L. Lv, Q. Li, Embedding CdS@Au into ultrathin $Ti_{3-x}C_2T_y$ to build dual Schottky barriers for photocatalytic H_2 production, ACS Catal. 11 (2021) 8510–8520, https://doi.org/10.1021/acscatal.1c02018.
[15] A.F. Alkaim, R. Dillert, D.W. Bahnemann, Effect of polar and movable (OH or NH_2 groups) on the photocatalytic H_2 production of alkyl-alkanolamine: a comparative study, Environ. Technol. 36 (2015) 2190–2197, https://doi.org/10.1080/09593330.2015.1024757.
[16] Z.C. Hu, X. Zhang, Q.W. Yin, X.C. Liu, X.F. Jiang, Z.M. Chen, X.Y. Yang, F. Huang, Y. Cao, Highly efficient photocatalytic hydrogen evolution from water-soluble conjugated polyelectrolytes, Nano Energy 60 (2019) 775–783, https://doi.org/10.1016/j.nanoen.2019.04.027.
[17] F. Qiu, Z.J. Han, J.J. Peterson, M.Y. Odoi, K.L. Sowers, T.D. Krauss, Photocatalytic hydrogen generation by CdSe/CdS nanoparticles, Nano Lett. 16 (2016) 5347–5352, https://doi.org/10.1021/acs.nanolett.6b01087.
[18] Y.G. Kim, W.K. Jo, Photodeposited-metal/CdS/ZnO heterostructures for solar photocatalytic hydrogen production under different conditions, Int. J. Hydrog. Energy 42 (2017) 11356–11363, https://doi.org/10.1016/j.ijhydene.2017.02.176.
[19] T. Wang, X.Q. Tao, X.L. Li, K. Zhang, S.J. Liu, B.X. Li, Synergistic Pd single atoms, clusters, and oxygen vacancies on TiO_2 for photocatalytic hydrogen evolution coupled with selective organic oxidation, Small 17 (2021) 2006255, https://doi.org/10.1002/smll.202006255.
[20] H. Liu, C.Y. Xu, D.D. Li, H.L. Jiang, Photocatalytic hydrogen production coupled with selective benzylamine oxidation over MOF composites, Angew. Chem. Int. Ed. 57 (2018) 5379–5383, https://doi.org/10.1002/anie.201800320.
[21] M. Bellardita, E.I. Garcia-Lopez, G. Marci, I. Krivtsov, J.R. Garcia, L. Palmisano, Selective photocatalytic oxidation of aromatic alcohols in water by using P-doped g-C_3N_4, Appl. Catal. B: Environ. 220 (2018) 222–233, https://doi.org/10.1016/j.apcatb.2017.08.033.
[22] X.L. Chen, Y. Kuwahara, K. Mori, C. Louis, H. Yamashita, A hydrophobic titanium doped zirconium-based metal organic framework for photocatalytic hydrogen peroxide production in a two-phase system, J. Mater. Chem. A 8 (2020) 1904–1910, https://doi.org/10.1039/c9ta11120d.
[23] Z.G. Chai, T.T. Zeng, Q. Li, L.Q. Lu, W.J. Xiao, D.S. Xu, Efficient visible light-driven splitting of alcohols into hydrogen and corresponding carbonyl compounds over a Ni-modified CdS photocatalyst, J. Am. Chem. Soc. 138 (2016) 10128–10131, https://doi.org/10.1021/jacs.6b06860.
[24] X.J. Ye, Y.H. Chen, Y.H. Wu, X.M. Zhang, X.C. Wang, S.F. Chen, Constructing a system for effective utilization of photogenerated electrons and holes: photocatalytic selective transformation of aromatic alcohols to aromatic aldehydes and hydrogen evolution over $Zn_3In_2S_6$ photocatalysts, Appl. Catal. B: Environ. 242 (2019) 302–311, https://doi.org/10.1016/j.apcatb.2018.10.004.
[25] U.R. Pillai, E. Sahle-Demessie, Oxidation of alcohols over Fe^{3+}/montmorillonite-K10 using hydrogen peroxide, Appl. Catal. A: Gen. 245 (2003) 103–109, https://doi.org/10.1016/S0926-860X(02)00617-8.
[26] T.P.A. Ruberu, N.C. Nelson, I.I. Slowing, J. Vela, Selective alcohol dehydrogenation and hydrogenolysis with semiconductor-metal photocatalysts: toward solar-to-chemical energy conversion of biomass-relevant substrates, J. Phys. Chem. Lett. 3 (2012) 2798–2802, https://doi.org/10.1021/jz301309d.
[27] P.X. Li, H. Zhao, X.Y. Yan, X. Yang, J.J. Li, S.Y. Gao, R. Cao, Visible-light-driven photocatalytic hydrogen production coupled with selective oxidation of benzyl alcohol over CdS@MoS_2 heterostructures, Sci. China Mater. 63 (2020) 2239–2250, https://doi.org/10.1007/s40843-020-1448-2.
[28] T.R. Chen, M.Q. Li, L.J. Shen, M.B.J. Roeffaers, B. Weng, H.X. Zhu, Z.H. Chen, D. Yu, X.Y. Pan, M.Q. Yang, Q.R. Qian, Photocatalytic anaerobic oxidation of aromatic alcohols coupled with H_2 production over $CsPbBr_3$/GO-Pt catalysts, Front. Chem. 10 (2022), 833784, https://doi.org/10.3389/fchem.2022.833784.
[29] S.G. Meng, X.J. Ye, J.H. Zhang, X.L. Fu, S.F. Chen, Effective use of photogenerated electrons and holes in a system: photocatalytic selective oxidation of aromatic alcohols to aldehydes and hydrogen production, J. Catal. 367 (2018) 159–170, https://doi.org/10.1016/j.jcat.2018.09.003.
[30] G. Shu, Y.D. Li, Z. Wang, J.X. Jiang, F. Wang, Poly(dibenzothiophene-S,S-dioxide) with visible light-induced hydrogen evolution rate up to 44.2 mmol h^{-1} g^{-1} promoted by K_2HPO_4, Appl. Catal. B: Environ. 261 (2020), 118230, https://doi.org/10.1016/j.apcatb.2019.118230.
[31] G. Shu, Y. Wang, Y.D. Li, S. Zhang, J.X. Jiang, F. Wang, A high performance and low cost poly(dibenzothiophene-S,S-dioxide)@TiO_2 composite with hydrogen evolution rate up to 51.5 mmol h^{-1} g^{-1}, J. Mater. Chem. A 8 (2020) 18292–18301, https://doi.org/10.1039/d0ta06159j.
[32] J. Thote, H.B. Aiyappa, A. Deshpande, D.D. Diaz, S. Kurungot, R. Banerjee, A covalent organic framework-cadmium sulfide hybrid as a prototype photocatalyst for visible-light-driven hydrogen production, Chem. Eur. J. 20 (2014) 15961–15965, https://doi.org/10.1002/chem.201403800.
[33] I.I., I.F. Perepichka, M.R. Perepichka, L.O.Palsson Bryce, Dibenzothiophene-S,S-dioxide-fluorene co-oligomers stable, highly-efficient blue emitters with improved electron affinity, Chem. Commun. (2005) 3397–3399, https://doi.org/10.1039/b417717g.
[34] Y.X. Liu, J. Wu, F. Wang, Dibenzothiophene-S,S-dioxide-containing conjugated polymer with hydrogen evolution rate up to 147 mmol g^{-1} h^{-1}, Appl. Catal. B: Environ. 307 (2022), 121144, https://doi.org/10.1016/j.apcatb.2022.121144.
[35] A. Kay, I. Cesar, M. Gratzel, New benchmark for water photooxidation by nanostructured alpha-Fe_2O_3 films, J. Am. Chem. Soc. 128 (2006) 15714–15721, https://doi.org/10.1021/ja064380l.
[36] K. Sivula, F. Le Formal, M. Gratzel, Solar water splitting: progress using hematite (alpha-Fe_2O_3) photoelectrodes, ChemSusChem 4 (2011) 432–449, https://doi.org/10.1002/cssc.201000416.
[37] J.X. Low, J.G. Yu, M. Jaroniec, S. Wageh, A.A. Al-Ghamdi, Heterojunction photocatalysts, Adv. Mater. 29 (2017) 1601694, https://doi.org/10.1002/adma.201601694.
[38] Y. Sasaki, H. Nemoto, K. Saito, A. Kudo, Solar water splitting using powdered photocatalysts driven by Z-schematic interparticle electron transfer without an electron mediator, J. Phys. Chem. C 113 (2009) 17536–17542, https://doi.org/10.1021/jp907128k.
[39] M.E. Aguirre, R.X. Zhou, A.J. Eugene, M.I. Guzman, M.A. Grela, Cu_2O/TiO_2 heterostructures for CO_2 reduction through a direct Z-scheme: protecting Cu_2O from photocorrosion, Appl. Catal. B: Environ. 217 (2017) 485–493, https://doi.org/10.1016/j.apcatb.2017.05.058.
[40] Z.F. Jiang, W.M. Wan, H.M. Li, S.Q. Yuan, H.J. Zhao, P.K. Wong, A hierarchical Z-Scheme alpha-Fe_2O_3/g-C_3N_4 hybrid for enhanced photocatalytic CO_2 reduction, Adv. Mater. 30 (2018) 1706108, https://doi.org/10.1002/adma.201706108.
[41] H. Chai, L.L. Gao, P. Wang, F. Li, G.W. Hu, J. Jin, In_2S_3/F-Fe_2O_3 type-II heterojunction bonded by interfacial S-O for enhanced charge separation and transport in photoelectrochemical water oxidation, Appl. Catal. B: Environ. 305 (2022), 121011, https://doi.org/10.1016/j.apcatb.2021.121011.
[42] A.W. Wang, J.X. Ni, W. Wang, X.Y. Wang, D.M. Liu, Q. Zhu, MOF-derived N-doped ZnO carbon skeleton@hierarchical Bi_2MoO_6 S-scheme heterojunction for photodegradation of SMX: mechanism, pathways and DFT calculation, J. Hazard. Mater. 426 (2022), 128106, https://doi.org/10.1016/j.jhazmat.2021.128106.
[43] M.M. Han, L.L. Hu, Y.J. Zhou, S.Q. Zhao, L. Bai, Y. Sun, H. Huang, Y. Liu, Z. H. Kang, Z-Scheme in a $Co_3(PO_4)(2)$/alpha-Fe_2O_3 photocatalysis system for overall water splitting under visible light, Catal. Sci. Technol. 8 (2018) 840–846, https://doi.org/10.1039/c7cy02323e.
[44] J. Kosco, M. Sachs, R. Godin, M. Kirkus, L. Francas, M. Bidwell, M. Qureshi, D. Anjum, J.R. Durrant, I. McCulloch, The effect of residual palladium catalyst contamination on the photocatalytic hydrogen evolution activity of conjugated polymers, Adv. Energy Mater. 8 (2018), 180218, https://doi.org/10.1002/aenm.201802181.
[45] F.S. Xing, R.Y. Zeng, C.C. Cheng, Q.W. Liu, C.J. Huang, POM-incorporated $ZnIn_2S_4$ Z-scheme dual-functional photocatalysts for cooperative benzyl alcohol oxidation and H_2 evolution in aqueous solution, Appl. Catal. B: Environ. 306 (2022), 121087, https://doi.org/10.1016/j.apcatb.2022.121087.
[46] Y.X. Li, K. Zhang, S.Q. Peng, G.X. Lu, S.B. Li, Photocatalytic hydrogen generation in the presence of ethanolamines over Pt/$ZnIn_2S_4$ under visible light irradiation, J. Mol. Catal. A: Chem. 363 (2012) 354–361, https://doi.org/10.1016/j.molcata.2012.07.011.
[47] K.N. Van, H.T. Huu, V.N.N. Thi, T.L.L. Thi, D.H. Truong, T.T. Truong, N.N. Dao, V. Vo, D.L. Tran, Y. Vasseghian, Facile construction of S-scheme SnO_2/g-C_3N_4 photocatalyst for improved photoactivity, Chemosphere 289 (2022), 133120, https://doi.org/10.1016/j.chemosphere.2021.133120.

[48] M. Mishra, D.M. Chun, alpha-Fe_2O_3 as a photocatalytic material: a review, Appl. Catal. A: Gen. 498 (2015) 126–141, https://doi.org/10.1016/j.apcata.2015.03.023.
[49] C. Cheng, B.W. He, J.J. Fan, B. Cheng, S.W. Cao, J.G. Yu, An inorganic/organic S-scheme heterojunction H_2-production photocatalyst and its charge transfer mechanism, Adv. Mater. 33 (2021) 2100317, https://doi.org/10.1002/adma.202100317.
[50] Y. Nosaka, A.Y. Nosaka, Generation and detection of reactive oxygen species in photocatalysis, Chem. Rev. 117 (2017) 11302–11336, https://doi.org/10.1021/acs.chemrev.7b00161.
[51] X.W. Shi, M. Fujitsuka, Z.Z. Lou, P. Zhang, T. Majima, In situ nitrogen-doped hollow-TiO_2/g-C_3N_4 composite photocatalysts with efficient charge separation boosting water reduction under visible light, J. Mater. Chem. A 5 (2017) 9671–9681, https://doi.org/10.1039/c7ta01888f.
[52] D.C. Jiang, X. Chen, Z. Zhang, L. Zhang, Y. Wang, Z.J. Sun, R.M. Irfan, P.W. Du, Highly efficient simultaneous hydrogen evolution and benzaldehyde production using cadmium sulfide nanorods decorated with small cobalt nanoparticles under visible light, J. Catal. 357 (2018) 147–153, https://doi.org/10.1016/j.jcat.2017.10.019.